1999

Warm Water Formation and Escape in the Upper Tropical Atlantic Ocean - 2. A Numerical Model Study

Sang-Ki Lee
Old Dominion University

G. T. Csanady
Old Dominion University

Original Publication Citation

Lee, S. K., & Csanady, G. T. (1999). Warm water formation and escape in the upper tropical Atlantic Ocean - 2. A numerical model study. *Journal of Geophysical Research: Oceans, 104*(C12), 29573-29590. doi:10.1029/1999jc900078

JOURNAL OF GEOPHYSICAL RESEARCH, VOL. 104, NO. C12, PAGES 29,573–29,590, DECEMBER 15, 1999

Warm water formation and escape in the upper tropical Atlantic Ocean
2. A numerical model study

Sang-Ki Lee[1] and G. T. Csanady[2]

Center for Coastal Physical Oceanography, Old Dominion University, Norfolk, Virginia

Abstract. We seek the simplest mass and heat balance scenario within the upper tropical Atlantic Ocean using a 2.5-layer numerical model, with the help of a newly suggested entrainment formula. The model ocean is driven by the seasonal wind and heat flux associated with the movement of the Intertropical Convergence Zone (ITCZ). The entrainment rate is scaled by the product of wind stress and shear at the bottom of the mixed layer. On an annual average, the northward transport of the tropical warm water is about 11 Sv, with roughly 10 Sv associated with entrainment of upper thermocline water. Out of the total 10 Sv of the needed upper thermocline water, 9 Sv enters the equatorial cell from the South Atlantic. The seasonal response to the ITCZ movement is most striking in the entrainment rate and the northward warm water escape rate. The entrainment is significant during May/December and ceases between January and March. The locally forced equilibrium response between the interface shear and the zonal wind stress east of 30°W appears to be responsible for this cycle. The warm water escape toward the North Atlantic takes place mainly from October to June and nearly stops during July/September. As a result of seasonal variations of the two key processes, namely, the entrainment and the northward warm water escape, the tropical warm water pool stores heat during May/October and lets heat escape in November/April.

1. Introduction

The dynamical connections within the equatorial current system have been demonstrated by *Cane* [1979]. The 2.5-layer tropical ocean model underlying his study, driven only by a constant zonal wind stress, reproduced the mass transport from the Equatorial Undercurrent (EUC) to the South Equatorial Current (SEC), linked by the equatorial entrainment.

Although this simple model calculation provided a first-order mass balance in the equatorial ocean, a few unrealistic assumptions were made to simplify the modeling procedure. For instance, the mixed layer depth was assumed constant, therefore no additional equation was used to estimate the entrainment rate at the interface. In addition, complications arising from the thermodynamics were avoided by assuming constant temperature in both layers. As an attempt to overcome these shortcomings, a more complex model was proposed by *Schopf and Cane* [1983]. The model included the mixed and thermocline layers. The entrainment (and detrainment) rate was determined from the *Kraus and Turner* [1967] model, where wind stress is the only source for turbulent mixing. The model was tested with constant easterly winds in a closed basin. The results showed that the mixed layer near the equator quickly reached a prescribed minimum depth and the entrainment rate was determined by the momentum divergence of the mixed layer thereafter. Eventually, the water accumulated in the mixed layer within the equatorial region, until the numerical model failed.

The failure of their model is due to two reasons, which must be taken into account in future tropical ocean modeling. First, mass balance cannot be achieved within the tropical ocean alone because mass exchange with the subtropical ocean is a critical factor. Similarly to *Schopf and Cane* [1983], *McCreary and Yu* [1992] modeled the mass balance via the meridional convective cell within the tropical ocean. However, this approach is far from realistic, since the strong heat flux at the sea surface does not allow detrainment to occur in the tropics.

[1]Now at Maritime Research Institute, Samsung Heavy Industries, Kyungnam, Korea.

[2]Now at Green Valley, Arizona.

Paper number 1999JC900078.
0148-0227/99/1999JC900078$09.00

Second, Kraus and Turner's [1967] model is not adequate for parameterizing the equatorial entrainment process. In other words, the local wind stress at the equator alone does not provide enough turbulent energy for the equatorial entrainment. Therefore the necessary turbulent energy must come from other mechanisms. The other conceivable source of turbulent energy in the equatorial region is the interface shear between the Equatorial Undercurrent and the South Equatorial Current [*Voituriez and Herbland*, 1979]. It is therefore necessary to parameterize the entrainment rate as functions of the turbulent energy production by both the wind and the interface shear. An entrainment formula suggested by *Jones and Mulhearn* [1983] appears to be a promising one, since their underlying assumption was based on the same idea. Yet another formula follows from the simple physical idea that the rate of turbulence energy production in the thermocline is stress times strain. An analysis of laboratory observations by *Lofquist* [1960] showed that a fraction of this turbulence energy is reconverted into mean potential energy, at the rate

$$w_e g' = \nu u^{*2} \left.\frac{du}{dz}\right|_0, \tag{1}$$

where ν is the efficiency of energy conversion, approximately equal to 0.03 [*Csanady*, 1978], and $du/dz|_0$ is the shear at the center of the thermocline. An alternative way of writing this is

$$w_e g' = \gamma \frac{u^{*2}|\triangle u|}{H}, \tag{2}$$

if γ is the entrainment coefficient and the layer scale is taken to be the mixed layer depth and the shear stress at the thermocline is proportional to wind stress (see section 2.1 for variable definitions). This should be a useful formula for parameterizing the equatorial entrainment rate, since it includes contributions both from wind stirring and interface shear. Previously, a mixed layer model similar to this but with much more complicated numerical procedure was applied to the equatorial ocean by *Chen et al.* [1994].

In this study, a simple 2.5-layer numerical model is formulated based on that of *Schopf and Cane* [1983] and is used to illustrate the warm water formation and escape process in the upper tropical Atlantic Ocean. The primary objective is to provide the simplest mass and heat balance scenario connecting the upper tropical Atlantic Ocean response to ITCZ movement. We also adopt the new entrainment formula suggested above.

The paper is organized in the following manner. The model equations and details of the numerical formulations are given in section 2. Section 3 presents the model results and discussion. The model results are summarized and conclusions are drawn in section 4.

2. Model Formulation

2.1. Governing Equations

Consider an ocean consisting of two active layers, a surface mixed layer and a thermocline layer as illustrated in Figure 1. The deep fluid below the thermocline layer is assumed to be stagnant (the reduced gravity approximation; see *Cushman-Roisin* [1994] for in-depth discussion). Let the longitude and latitude be given by ϕ and θ, respectively, then the depth-integrated momentum, continuity, and heat conservation equations for the mixed layer are

$$\frac{\partial(u_1 h_1)}{\partial t} + \frac{1}{a\cos\theta}\frac{\partial}{\partial\phi}(u_1^2 h_1) + \frac{1}{a}\frac{\partial}{\partial\theta}(u_1 v_1 h_1) - 2\frac{u_1 v_1 h_1}{a}\tan\theta - 2\Omega\sin\theta v_1 h_1 = \frac{-h_1}{\rho_1 a\cos\theta}\frac{\partial p_1}{\partial\phi} + \frac{\tau^{(\phi)}}{\rho_1} + w_e u_2 - K(u_1 - u_2) + F_{1\phi} \tag{3}$$

$$\frac{\partial(v_1 h_1)}{\partial t} + \frac{1}{a\cos\theta}\frac{\partial}{\partial\phi}(u_1 v_1 h_1) + \frac{1}{a}\frac{\partial}{\partial\theta}(v_1^2 h_1) + \frac{(u_1^2 - v_1^2)h_1}{a}\tan\theta + 2\Omega\sin\theta u_1 h_1 = \frac{-h_1}{\rho_1 a}\frac{\partial p_1}{\partial\theta} + \frac{\tau^{(\theta)}}{\rho_1} + w_e v_2 - K(v_1 - v_2) + F_{1\theta} \tag{4}$$

$$\frac{\partial h_1}{\partial t} + \frac{1}{a\cos\theta}\left[\frac{\partial u_1 h_1}{\partial\phi} + \frac{\partial}{\partial\theta}(v_1 h_1\cos\theta)\right] = w_e, \tag{5}$$

$$\frac{\partial T_1}{\partial t} + \frac{u_1}{a\cos\theta}\frac{\partial T_1}{\partial\phi} + \frac{v_1}{a}\frac{\partial T_1}{\partial\theta} = \frac{Q}{\rho C_{pw} h_1} - \frac{w_e}{h_1}(T_1 - T_2) + K_h\nabla^2 T_1, \tag{6}$$

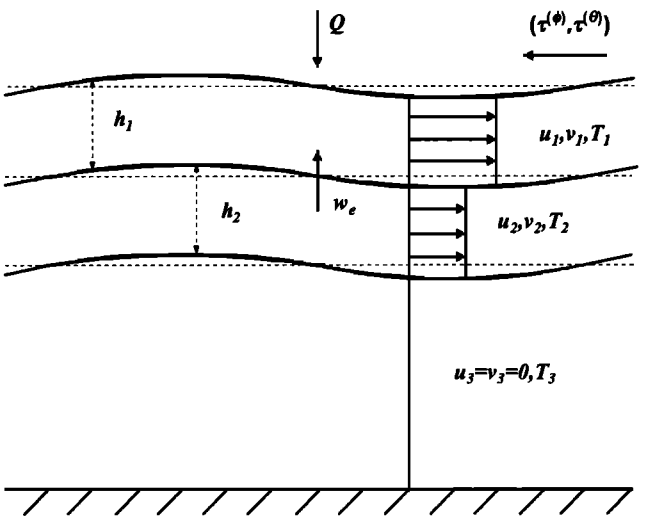

Figure 1. Model configuration and vertical structure of temperature and velocity assumed in the model equations.

and for the thermocline layer:

$$\frac{\partial(u_2h_2)}{\partial t}+\frac{1}{a\cos\theta}\frac{\partial}{\partial\phi}(u_2^2h_2)+\frac{1}{a}\frac{\partial}{\partial\theta}(u_2v_2h_2)$$
$$-2\frac{u_2v_2h_2}{a}\tan\theta-2\Omega\sin\theta v_2h_2=\frac{-h_2}{\rho_2 a\cos\theta}\frac{\partial p_2}{\partial\phi}$$
$$-w_eu_2+K(u_1-u_2)+F_{2\phi} \quad (7)$$

$$\frac{\partial(v_2h_2)}{\partial t}+\frac{1}{a\cos\theta}\frac{\partial}{\partial\phi}(u_2v_2h_2)+\frac{1}{a}\frac{\partial}{\partial\theta}(v_2^2h_2)$$
$$+\frac{(u_2^2-v_2^2)h_2}{a}\tan\theta+2\Omega\sin\theta u_2h_2=\frac{-h_2}{\rho_2 a}\frac{\partial p_2}{\partial\theta}$$
$$-w_ev_2+K(v_1-v_2)+F_{2\theta} \quad (8)$$

$$\frac{\partial h_2}{\partial t}+\frac{1}{a\cos\theta}\left[\frac{\partial u_2h_2}{\partial\phi}+\frac{\partial}{\partial\theta}(v_2h_2\cos\theta)\right]=-w_e, \quad (9)$$

$$\frac{\partial T_2}{\partial t}=0, \quad (10)$$

where the horizontal friction terms for the jth layer are [*Gill*, 1982]

$$F_{j\phi}=A_hh_j(\nabla^2u_j-\frac{u_j}{a^2\cos^2\theta}-\frac{2\sin\theta}{a^2\cos^2\theta}\frac{\partial v_j}{\partial\phi}), \quad (11)$$

$$F_{j\theta}=A_hh_j(\nabla^2v_j-\frac{v_j}{a^2\cos^2\theta}+\frac{2\sin\theta}{a^2\cos^2\theta}\frac{\partial u_j}{\partial\phi}). \quad (12)$$

On the basis of the hydrostatic relation, the pressure gradient terms are given by

$$\nabla p_1=g\alpha\nabla[h_1(T_1-T_3)+h_2(T_2-T_3)]$$
$$-{}^1\!/_2 g\alpha h_1\nabla T_1, \quad (13)$$

$$\nabla p_2=g\alpha\nabla[(h_1+h_2)(T_2-T_3)], \quad (14)$$

where the buoyancy is calculated only from a linear thermal expansion for simplicity. The entrainment rate is determined from a new formula described in the previous section, with the addition of a background dissipation term [*Kim*, 1976]:

$$w_e=\gamma\frac{u^{*2}|\Delta u|}{g'h_1}-\frac{2\epsilon_o}{g'}, \quad (15)$$

where γ is the entrainment coefficient, g' $[=g\alpha(T_1-T_2)]$ is the reduced gravity, ϵ_o is the dissipation coefficient, u^{*2} is the surface stress, and Δu is the mean shear:

$$\Delta u=\sqrt{(u_1-u_2)^2+(v_1-v_2)^2}. \quad (16)$$

The dissipation term gives the model an ability to terminate (or restart) the entrainment when the turbulence energy production is weak, at which time the mixed layer depth becomes

$$h_{\text{crit}}=\gamma\frac{u^{*2}|\Delta u|}{2\epsilon_o}. \quad (17)$$

Inclusion of the dissipation term appears to be realistic, since weak turbulence cannot be reconverted to mean potential energy but is prone to dissipation [*Kim*, 1976].

Variables used in (3)-(17) are defined as follows:

u_j,v_j	zonal and meridional components of velocity for layer j;
h_j	thickness of layer j;
T_j	temperature of layer j;
g	acceleration of gravity;
α	thermal expansion coefficient;
ρ_j	density of layer j;
p_j	pressure of layer j;
a	radius of the Earth;
Ω	angular velocity of rotation of the Earth;
$\tau^{(\phi)}$,$\tau^{(\theta)}$	zonal and meridional components of wind stress;
w_e	entrainment velocity across the interface;
A_h	Laplacian mixing coefficient for momentum;
K_h	Laplacian mixing coefficient for heat;
K	interfacial friction parameter;
Q	heat flux at the sea surface;
C_{pw}	specific heat of water.

2.2. Model Geometry and Boundary Conditions

The model covers the tropical Atlantic Ocean and some portion of the subtropical oceans of both hemispheres from 20°S to 20°N and 90°W to 15°E. The northern and southern boundaries are open. The Caribbean islands are all removed from the model geometry for simplicity. The model domain is not extended farther poleward to focus on the local response of the tropical Atlantic, minimizing the connection with remote parts of the ocean. In addition, a poleward extension of the model domain may introduce the need to parameterize midlatitude processes, such as detrainment, which may not be properly represented in the simple format of the current model.

At the wall boundaries, a no-slip boundary condition is applied. For the two openings at 20°N and 20°S, *Orlanski*'s [1976] radiation condition is used for u, v, and h variables in an implicit form suggested by *Chapman* [1985]. For the temperature variable T, a no-flux condition is applied at all walls and open boundaries. In order to allow realistic heat flux through the open boundaries, two narrow zonal sponge layers are placed from 15° to 20° in both hemispheres. The mixed layer temperature relaxes back to the monthly surface temperature data of *Levitus* [1982] inside the sponge layers (e-folding timescale of about 25 days). For the stability at the open boundaries, a one-dimensional *Hensen* [1962] filter is applied every 40 time steps to the two

rows nearest to the open boundaries for u, v, and h. In addition, the mixing coefficients, A_h and K for u_j, increase linearly (up to twice their values) inside the sponge layers from 15° to 20°. There is no corresponding treatment on v_j so that the fluid can pass freely across the open boundaries.

2.3. Numerical Formulation

The model equations (3)-(10) are discretized in space on an Arakawa C-grid scheme. The numerical scheme is the mass- and energy-conserving *Lilly* [1965] scheme (C scheme according to *Grammeltveldt* [1969]), with the exception of the Coriolis terms. *Holland and Lin*'s [1975] scheme is used for the Coriolis term. The grid size is 1° in both horizontal directions; therefore the model domain contains 106×41 grid points per layer for each variable. The leapfrog time integration scheme is used with a time step of about 1 hour. The *Shuman* [1957] averaging scheme is applied twice consecutively every 40 time steps to remove the computational mode produced by the leapfrog scheme, as suggested by *Killworth* [1984].

2.4. Surface Heat Flux and Wind Stress

The formula for thermal heat flux is based on the heat budget of the ocean [*Fleagle and Businger*, 1980], which can be written as

$$Q = Q_{\mathrm{SW}} - Q_{\mathrm{LW}} - Q_S - Q_E, \tag{18}$$

where Q is the net heat flux, Q_{SW} is the incoming short wave radiation, Q_{LW} is the back radiation (positive upward), Q_S is the sensible heat flux, and Q_E is the latent heat flux of evaporation. The bulk formula of sensible heat flux is

$$Q_S = \rho_a C_{pa} D_s |V| (T_1 - T_a), \tag{19}$$

where ρ_a is the density of air, C_{pa} is the specific heat of air, T_a is the air temperature, D_s is the dimensionless constant for heat conduction (or Stanton number), and $|V|$ is the wind speed. The formula for the latent heat flux of evaporation [*Haney*, 1971] is

$$Q_E = \rho_a D_d L |V| [e_s(T_1) - \varrho e_s(T_a)](0.622/P_a), \tag{20}$$

where P_a is the atmospheric pressure (in mbar), L is

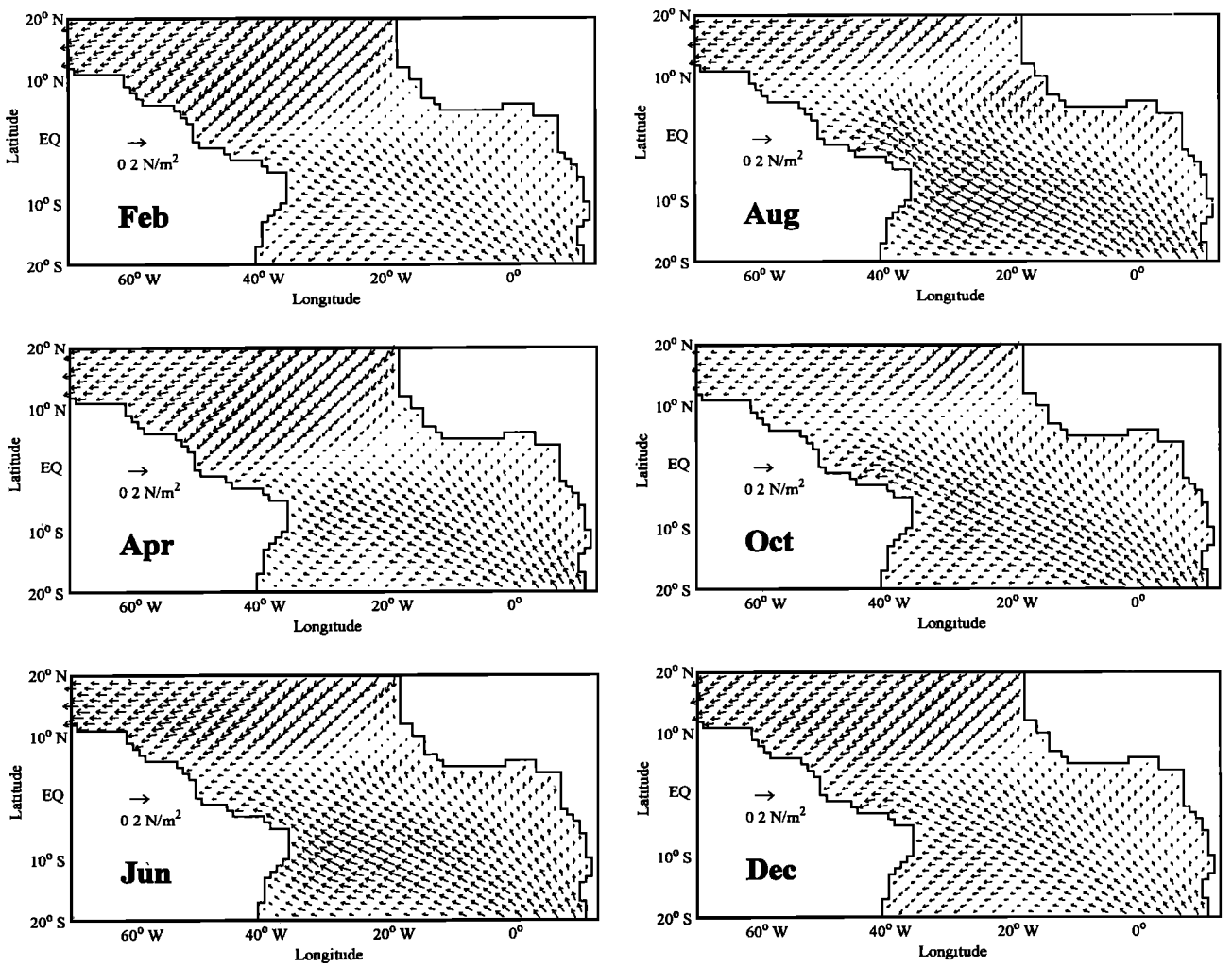

Figure 2. Monthly mean wind stress vectors from February to December (in units of N/m^2). Reproduced from *Hellerman and Rosenstein* [1983].

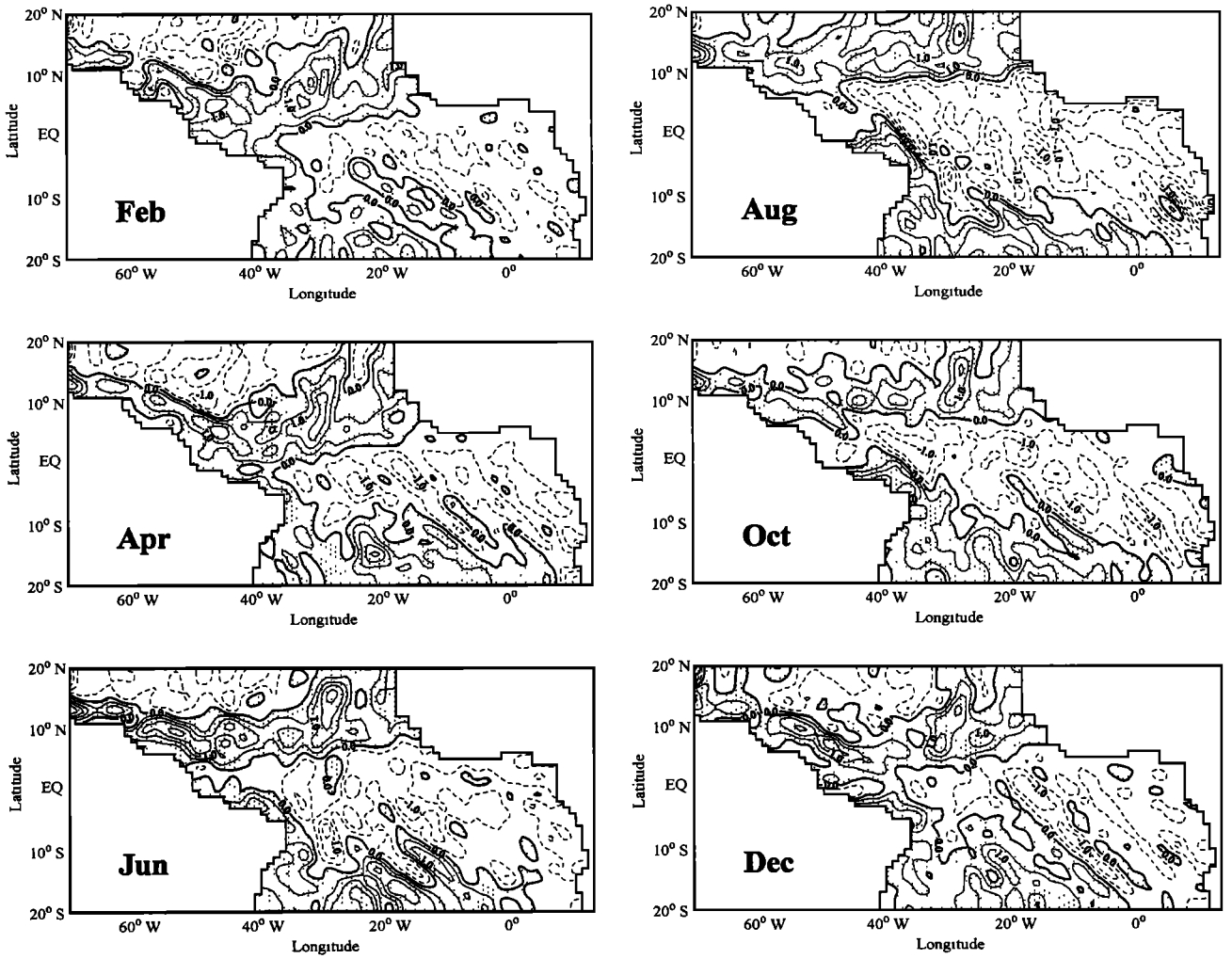

Figure 3. Monthly mean wind stress curls from February to December (in units of N/m^3). Positive wind stress curl is shaded. Reproduced from *Hellerman and Rosenstein*, [1983].

the latent heat of evaporation per unit mass, D_d is the dimensionless constant for evaporation (or Dalton number), ϱ is the relative humidity (dimensionless), and $e_s(T_1)$ and $e_s(T_a)$ are saturation vapor pressure at the sea surface and air (10 m above sea surface), respectively. The saturation vapor pressure (in mbar) for temperature between ± 40°C can be parameterized [*Gill*, 1982] by

$$\log_{10} e_s(T) = \frac{(0.7859 + 0.03477T)}{(1 + 0.00412T)}. \qquad (21)$$

The forcing variables (Q_{SW}, Q_{LW}, $|V|$, T_a) are obtained from *Esbensen and Kushnir* [1981]. A cubic spline interpolation is applied to the 12 monthly means of the data in order to match the model grid system (from 5° interval to 1°). Then these interpolated data are decomposed into five Fourier harmonics (12-, 6-, 4-, 3-, and 2.4-month periods) in time to provide a continuous time series for the model integration.

The model is forced by the climatological monthly mean wind stresses of *Hellerman and Rosenstein* [1983]. Similar to the heat flux variables, the cubic spline interpolation is applied to the 12 monthly means of wind stress data to match the model grid system (from 2° interval to 1°). Then they are decomposed into five Fourier harmonics (12-, 6-, 4-, 3-, and 2.4-month periods) in time to provide a continuous time series.

The monthly averaged wind stress and its curl over the tropical Atlantic Ocean are reproduced from *Hellerman and Rosenstein* [1983] in Figures 2 and 3, respectively. Associated with the movement of the ITCZ, the seasonal variation of tropical wind stress is highly concentrated inside the zonal band between 2°N and 10°N [*Servain and Legler*, 1986]. The wind stress inside this zonal band is relatively strong during northern summer, and its curl changes sign from positive to negative between April and August. It is noticeable that the wind stress pattern exhibits a significant variation in the zonal direction as well: the wind stress is stronger and generally zonal in the western equatorial region, while the eastern side is dominated by the meridional wind.

The parameter values used for the model integration are listed in Table 1. Unless specified otherwise, the

Table 1. Parameters used for model integration

Parameter	Notation	Value
H_1	initial thickness of layer 1	50 m
H_2	initial thickness of layer 2	150 m
T_1	initial temperature of layer 1	25.7°C
T_2	temperature of layer 2	20°C
T_3	temperature of layer 3	10°C
α	thermal expansion coefficient	$0.00025°C^{-1}$
A_h	Laplacian mixing coefficient for momentum	3500 m^2/s
K_h	Laplacian mixing coefficient for heat	3500 m^2/s
K	interfacial friction parameter	$8\times10^{-7}s^{-1}$
C_{pw}	specific heat of water	4200 J/kg/°C
C_{pa}	specific heat of air	1004 J/kg/°C
P_a	atmospheric pressure at 10 m from sea level	1013 mbar
ρ_a	air density	1.2 kg/m^3
ρ	water density	1020 kg/m^3
ϱ	relative humidity, dimensionless	0.8
L	latent heat of evaporation per unit mass	2.49×10^6 J/kg
D_s	Stanton number, dimensionless	1.5×10^{-3}
D_d	Dalton number, dimensionless	1.5×10^{-3}
γ	entrainment coefficient	1/12
ϵ_o	background dissipation of entrainment	7.5×10^{-9} m^2/s^3

values in Table 1 are all constant during the model integration.

2.5. Mass-Restoring Device

Schopf and Cane [1983] demonstrated that mass balance cannot be achieved within the tropical ocean itself, without mass exchange with the subtropical oceans. A typical way to incorporate the remote effect in the regional model is to fix the volume transport at the open boundaries [e.g., *Ezer and Meller*, 1997]. In this study, however, we take a different approach. We simply relax the layer depths slowly back to the initial depth profile inside the narrow sponge layers specified near the open boundaries (with an e-folding timescale of about 250 days). This scheme therefore provides the mass-restoring mechanism during the model integration. If the layer thickness becomes shallower than the initial value, a volume of water, proportional to the depth anomaly, is injected into the model domain at the open boundaries and vice versa.

Since the initial depth profile involves no zonal slope and hence no geostrophic meridional flow, this scheme at the open boundaries plays only a passive role. If not realistic, it still best fits the interest of this study, since we are mainly concerned with the local response of the tropical ocean and not with any remote effect from the higher-latitude oceans. In any case, without this mass-restoring mechanism, the mixed or thermocline layer may be completely depleted during the numerical integration, as happened in the model of *Schopf and Cane* [1983]. A procedure similar to this was employed previously by *Jensen* [1990] on the numerical simulation of the Somali Current.

3. Model Results and Discussion

The model was integrated from rest and run for about 15 years, at which time it reached a quasiperiodic state. This was determined by the fact that the model attained a quasiperiodic cycle in kinetic energy, as well as mass and heat budget. The results described here are based on the 16th year of the model simulation.

3.1. Annual Mean Mass and Heat Budget

Figure 4 shows schematic diagrams of the zonally integrated annual mean mass and heat transports at 8°S and 8°N. The top two bars represent the mixed and thermocline layer transports. The upward and downward arrows indicate the vertical transport via the equatorial entrainment and the surface heat flux, respectively. For better description of the total heat transport, the southward transport of North Atlantic Deep Water (NADW) required to balance the net northward mass transport of the upper ocean is included in Figures 4a and 4b. In order to estimate the total heat transport, a mean temperature of 7.5°C is assumed for the NADW. Associated total heat transport is indicated at the bottom of Figures 4a and 4b.

Figure 4a illustrates that 10 Sv of thermocline water enters the equatorial cell, with roughly 9 Sv com-

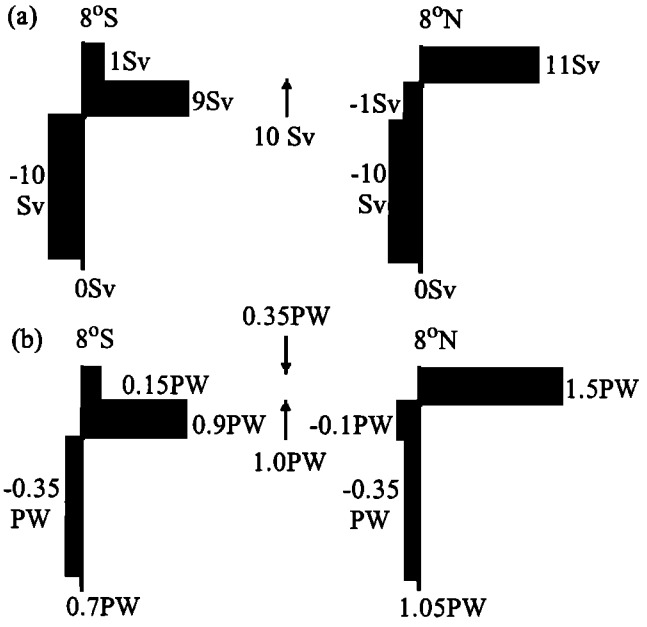

Figure 4. Annual mean (a) mass (in Sv) and (b) heat (in PW) transports across 8°S and 8°N. The top two bars represent the mixed and thermocline layer transports. The upward and downward arrows indicate the vertical transport via equatorial entrainment and surface heat flux, respectively. The imaginary southward transport of North Atlantic Deep Water (NADW) required for mass balance is included in the lowest bars.

ing from the South Atlantic and 1 Sv from the North Atlantic. This 10 Sv of upper thermocline water is entrained in the surface mixed layer. The entrained water then joins 1 Sv of surface water from the South Atlantic and flows into the North Atlantic across the equator. The estimated relative transport scales are in reasonable agreement with observations [e.g., *Roemmich*, 1983].

It can be seen that the heat flux across a given latitude is almost proportional to the mass flux. The reason is that the temperature variation is far smaller than the space-averaged temperature [*Philander and Pacanowski*, 1986]. Even so, some features of the heat transport pattern in Figure 4b are still worth mentioning. In the thermocline layer, about 0.9 PW (10^{15}W) of heat is transported to the equatorial cell across 8°S from the South Atlantic. A total of 1.0 PW of heat is transferred to the surface mixed layer via the equatorial entrainment. This cold, entrained water then gains about 0.35 PW of heat at the sea surface (warm water formation) and is carried away to the subtropical ocean in the North Atlantic. There are additional heat gains from the surface water of the South Atlantic (0.15 PW) and from the thermocline water of the North Atlantic (0.1 PW), but their contributions are not significant. Therefore, taking the NADW transport (−0.35 PW) into account, the total heat transports are 0.7 PW at 8°S and 1.05 PW at 8°N. The heat deficit between the two latitudes is added from the surface heat flux (0.35 PW). The total heat transport and surface heat flux values are in good agreement with the general circulation model (GCM) study of *Philander and Pacanowski* [1986]. However, the model underestimates the values obtained by the inverse calculation of *Roemmich* [1983]. He estimated about 0.74 and 1.61 PW at 8°S and 8°N, respectively, thereby a net heating of 0.87 PW at the sea surface. It must be noted, however, that not all estimates of heat transports in the tropical Atlantic are consistent with each other. For instance, using the heat budget equation, *Hastenrath* [1980] obtained about 1.25 and 1.5 PW at 10°S and 10°N, respectively, hence a net surface heating of 0.25 PW between the two latitudes; but, using the same method, *Hsiung* [1985] estimated 0.2 and 0.8 PW at 10°S and 10°N, respectively. In any case, the model-estimated 0.35 PW of oceanic heat gain between 8°S and 8°N falls inside the range between the *Hastenrath* [1980] and *Hsiung* [1985] estimations.

Figures 5a and 5b show the two-dimensional annual mean mass transport vectors for the mixed and ther-

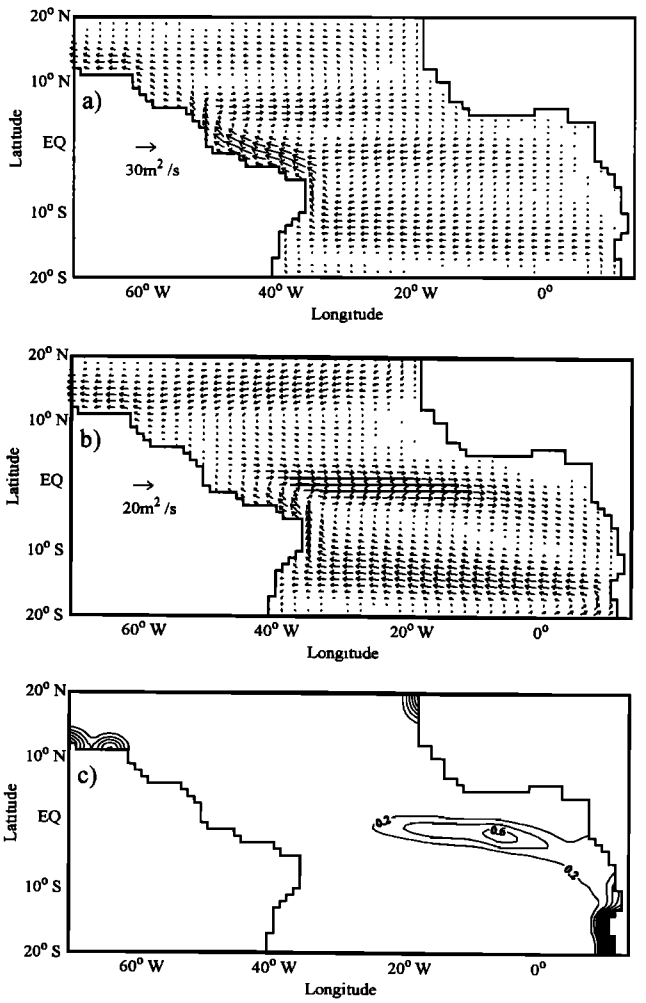

Figure 5. Annually averaged mass transport in (a) the mixed layer and (b) the thermocline layer (in m^2/s). (c) Annual mean entrainment rate (in 10^{-5}m/s).

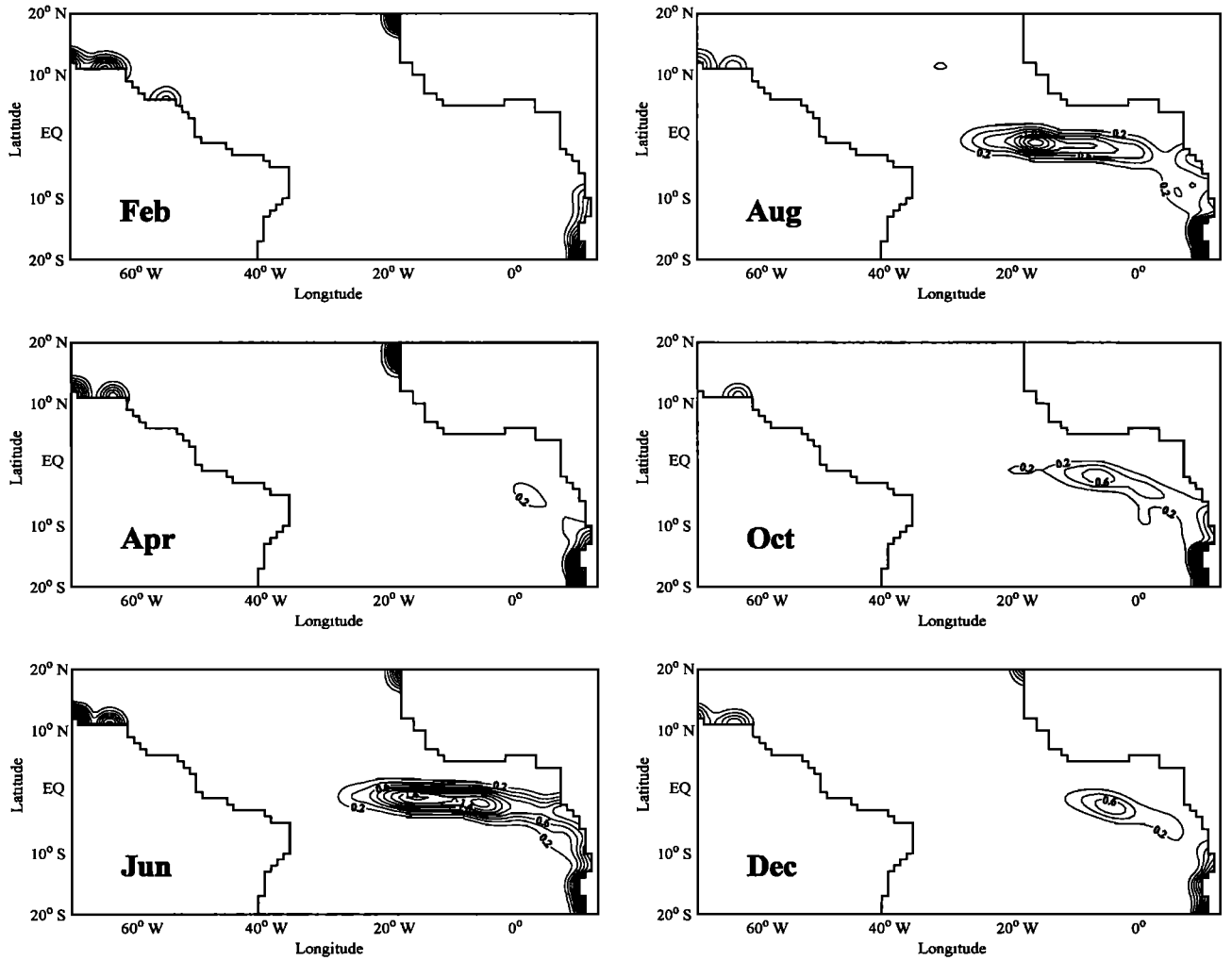

Figure 6. Monthly averaged entrainment rate from February to December from the model results. The unit is 10^{-5}m/s.

mocline layer, respectively. The vertical mass flux rate between the two layers is shown in Figure 5c. Figure 5 illustrates that the thermocline waters enter the model domain from the southeastern corner, cross the South Atlantic via the northern leg of the subtropical gyre, and then turn northward and feed the Equatorial Undercurrent. These cold, thermocline waters are then entrained at the central and eastern parts of the equator and transported to the west by the South Equatorial Current, thus escaping the equatorial region via the NBC. In turn, the NBC bifurcates into the Guiana Current and the North Equatorial Countercurrent (NECC). The Guiana Current continues northwestward along the western boundary. The NECC, on the other hand, joins the North Equatorial Current (NEC) via the cyclonic gyre located between the NECC and the NEC. Eventually, both branches join at the western boundary near 12°N and escape the model domain through the Caribbean Current. It is evident from Figure 5b that the subsurface subtropical waters of the North Atlantic hardly contribute to the Equatorial Undercurrent. The major route and the scale of the mass transport inside the equatorial cell agree well with the schematic pictures presented by *Csanady* [1987, 1990] and *Gouriou and Reverdin* [1992].

3.2. Seasonal Cycle of Mass and Heat Budget

The tropical Atlantic is subject to unusually high seasonal variation, presumably associated with the seasonal excursion of ITCZ. In this section, we investigate the seasonal cycle of the mass and heat budget from the model results, focusing on the budget near the equatorial region.

3.3. Equatorial Entrainment

Figure 6 shows the entrainment rate for February, April, June, August, October, and December. The entrainment near the equator nearly vanishes between February and April and suddenly starts after April in the eastern part of the equator. Within a month or so, it quickly extends toward the central basin up to

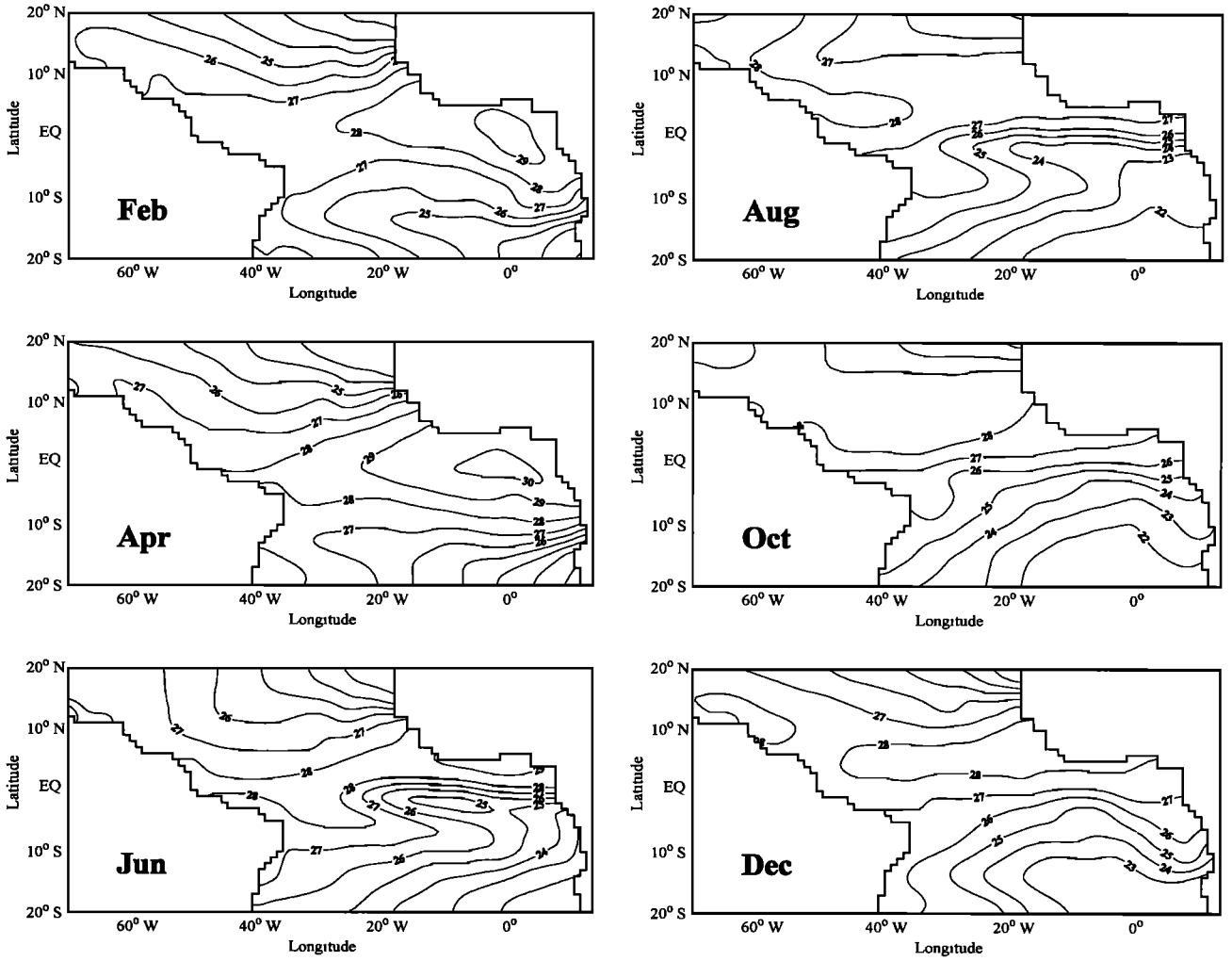

Figure 7. Monthly averaged sea surface temperature (SST) from February to December inferred from model results. The unit is °C.

25°W. Shortly after it reaches its peak ($\sim 1.5\times10^{-5}$ m/s at the core) in June, the entrainment rate starts to reduce and its center moves back toward the eastern basin. Entrainment lasts until December and dies out only in February. A prominent feature is that the entrainment is limited to the central and eastern basin, where the mixed layer depth is relatively shallow. It is also noticeable that the center of the entrainment is located slightly southward of the equator around 1°S - 2°S. Especially the eastern end is tilted much more toward the south and sometimes connected to the coastal entrainment zone off the west coast of South Africa in the South Atlantic.

Since the magnitude of the entrainment rate is too small to measure, no direct observation of entrainment rate is available to verify the model results. A more practical way of verification is to look at the SST variation, which can be roughly identified by the entrainment cycle. The monthly averaged SST from the model results is shown in Figure 7. The corresponding map of the observed SST taken from *Hastenrath and Lamb* [1978] is shown in Figure 8. Generally, there is good agreement between the model results and observations. The warm water pool (high SST) in the eastern equatorial cell is observed from February to April in both SST maps, and both show a sudden development of the cold water tongue in June and its intensification in August. An interesting point is that the maximum of the entrainment rate is in June/July, but the cold water tongue is most intense in August as shown in Figure 7. A loose explanation for this is that the entrainment of cold subsurface water is proportional to the time change of the SST (see (6)). Therefore the SST and the entrainment rate are not necessarily in phase. To fully understand the connection between the variations of the SST and the entrainment rate, the heat budget of the mixed layer must be examined. This subject is discussed in section 3.7.

3.4. Escape of the Warm Water Mass

Figure 9 shows the bimonthly map of the mixed layer mass transport from February to December. The trans-

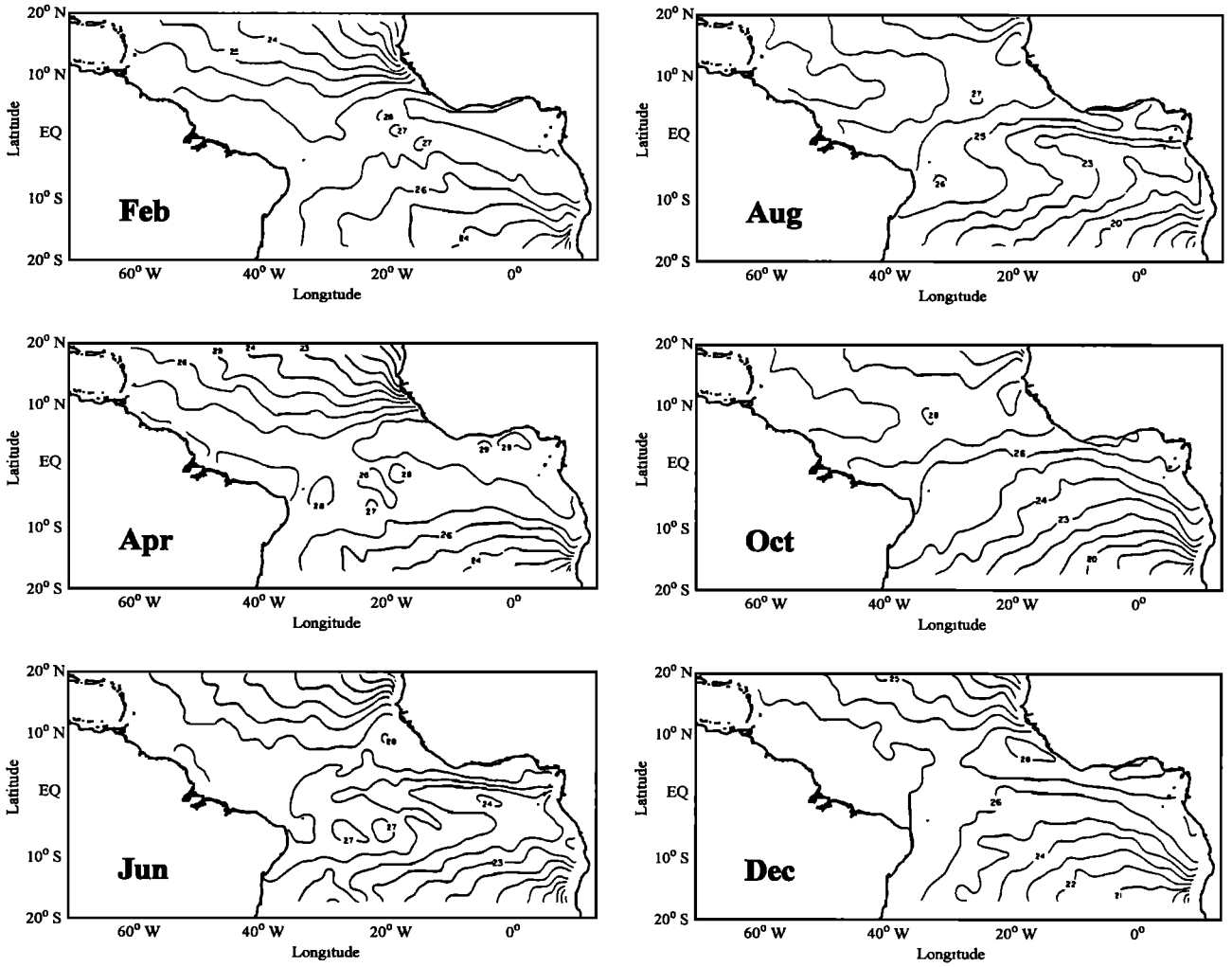

Figure 8. Monthly averaged SST (°C) from February to December from *Hastenrath and Lamb* [1978]. Reproduced by permission of The University of Wisconsin Press.

ports are averaged monthly; therefore the eddy transports are mostly averaged out. Continuation of the NBC to the Guiana Current is apparent in February. During April, the NEC, the southern leg of the subtropical gyre, moves down as far as 8°N and enhances the northwestward Guiana Current. In June, the NBC retroflects from the coast and feeds the eastward flowing NECC. At the same time, the northwestward mass transport via the NBC-Guiana Current system is reduced considerably. In August, the NBC turns completely offshore into the NECC and the northward flow from the NBC to the Guiana Current nearly vanishes. After October, the NECC becomes weaker and the mass transport through the NBC-Guiana Current system increases again. The escape of the warm water mass (WWM) via this route becomes a maximum in February when the NECC practically dies out. This portion of the model result agrees well with the recent observational study of *Johns et al.* [1998] and GCM models [*Sarmiento*, 1986; *Philander and Pacanowski*, 1986], which are discussed in detail by Lee and Csanady [this issue] (hereafter refered to as part 1).

Figure 9 shows that there is a secondary route of WWM escape from the NBC to the NEC, via the interior of the cyclonic gyre as pointed out by *Csanady* [1990]. The cyclonic gyre is driven by a band of positive wind stress curl, which exists between the equator and 10°N in April and between 10°N to 20°N in August (see Figure 3). The meridional WWM transport across 8°N, shown in Figure 10, illustrates that the escape of the WWM via this route takes place during October/June. During these months, as stated by *Csanady* [1990], since the western boundary current (WBC) off the Guiana coast always flows northwestward, the interior northward transport comes from the residual NECC. When the NECC is weakened in February/April, the northward mass transport is supplied by a weak effluent of the NBC, which takes the place of the NECC. In contrast to October/June, the meridional transport is completely blocked in July/September (Figure 10). As stated in part 1, the cyclonic gyre is in Sverdrup balance, which may be separated into the Ekman and geostrophic parts. Further analysis shows that the seasonal variation of the interior mass transport is domi-

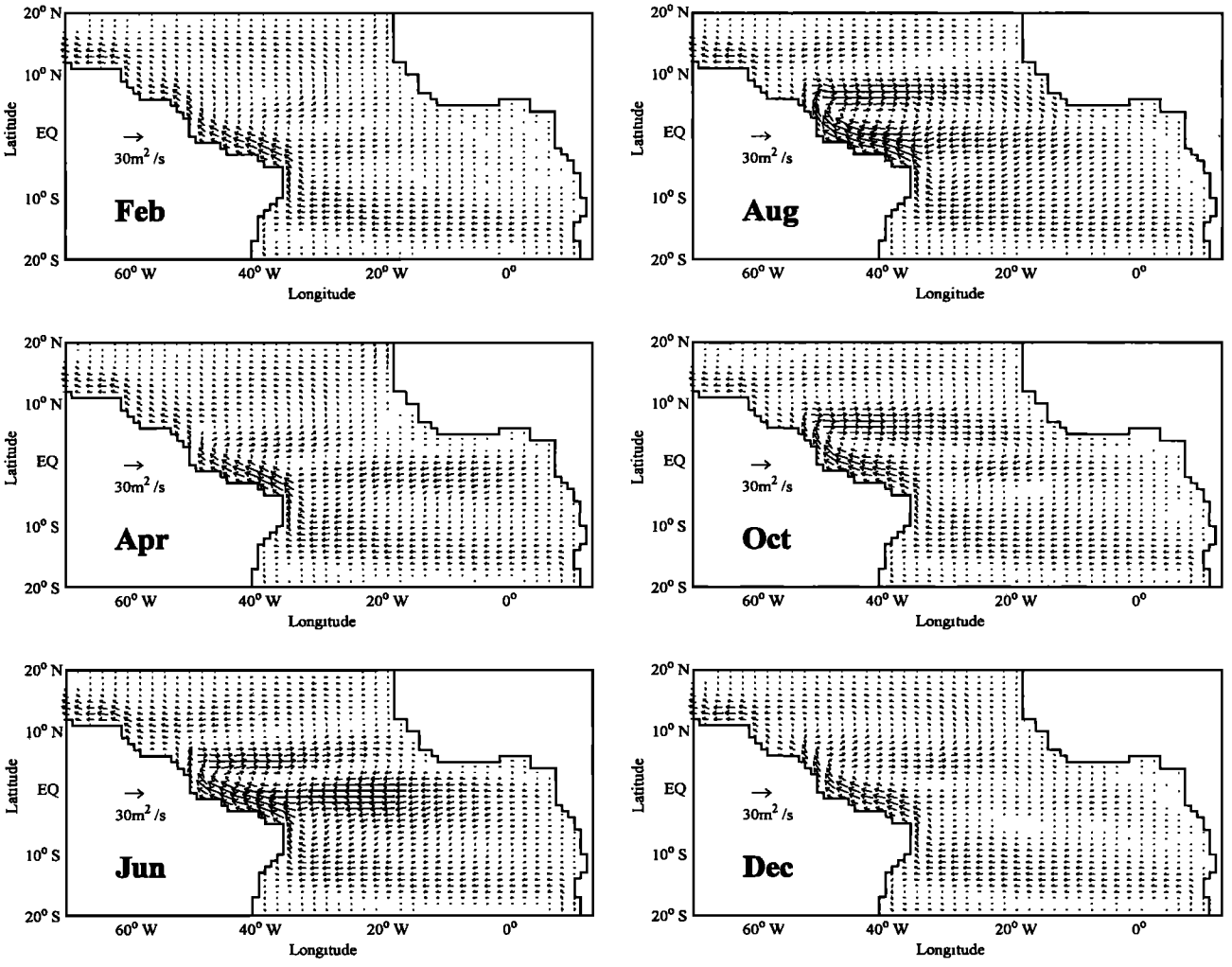

Figure 9. Monthly averaged mass transport (m^2/s) in the mixed layer from February to December inferred from the model result.

nated by the Ekman transport. See *Lee* [1995] for further details.

3.5. Transport in the Thermocline Layer

The mass transport in the thermocline layer from February to December is shown in Figure 11. It appears that the EUC is the only source of major seasonal variation. Therefore the equatorial zonal mass transports across 30°W, 20°W, and 10°W are contoured in Figure 12. The zonal transport across 30°W is relatively small during February/April. After April, it starts to increase until it reaches its maximum in July and decreases thereafter. At 20°W, the EUC transport pattern is very similar to that across 30°W, but the maximum transport occurs in September/October and the core of the EUC is shifted slightly southward. The EUC transport is reduced significantly at 10°W, the maximum transport is in October, and its core is shifted farther south, particularly in October/April.

Figure 13 shows the meridional mass transport in the thermocline layer across 8°S as a function of time and longitude. The subsurface NBC experiences no significant seasonal changes. Meanwhile, the transport in the eastern basin is dominated by its seasonal cycle. It appears that the variability in the east is created by the surplus of the EUC transport during September/May, when the equatorial entrainment is not significant.

3.6. Seasonal Storage Rate of Mass and Heat

The storage rate of the WWM inside the equatorial belt is defined here as the sum of entrainment and horizontal flux rate across the two zonal boundaries at 8°S and 8°N, separately for the two active layers of the model. Therefore, in order to quantify the seasonal cycle of the WWM storage rate, the entrainment rate is integrated between 8°N and 8°S and the meridional transports of the WWM are integrated along 8°S and 8°N as shown in Figures 14a and 14b. The WWM storage rate is obtained by summing these three components as shown in Figure 14c. The entrainment rate reaches up to 25 Sv in June and decreases rapidly until October. A minor peak of 8 Sv is observed in Novem-

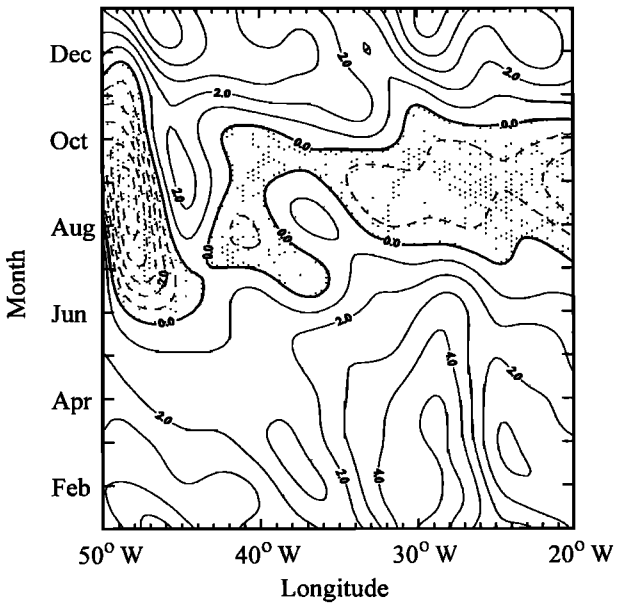

Figure 10. Time-longitude plot of the total meridional transport in the mixed layer across 8°N. The shaded area is negative (southward), and the unit is m^2/s.

ber. The horizontal mass flux across 8°S is insignificant in the mixed layer. The storage rate of the WWM (i.e., the mixed layer net storage) is therefore largely determined by the interplay between the entrainment rate and the northward escape across 8°N, as suggested by *Csanady* [1987]. Between January and April, the entrainment nearly ceases, while the northward escape reaches its maximum of 19 Sv. During May/December, on the contrary, the entrainment becomes significant but the northward escape is minimal. Consequently, the WWM inside the equatorial belt is depleted during November/April and accumulates between May and October, as depicted in Figure 14c. The maximum accumulation occurs in July, as the entrainment rate has its maximum at June and the northward escape rate has its minimum in August. The storage rate in the thermocline layer is, on the other hand, determined solely by the entrainment rate, since the fluxes across 8°N or 8°S show no significant seasonal changes (see Figures 14b and 14c). The two-dimensional pattern of the WWM storage rate is discussed by *Lee* [1995].

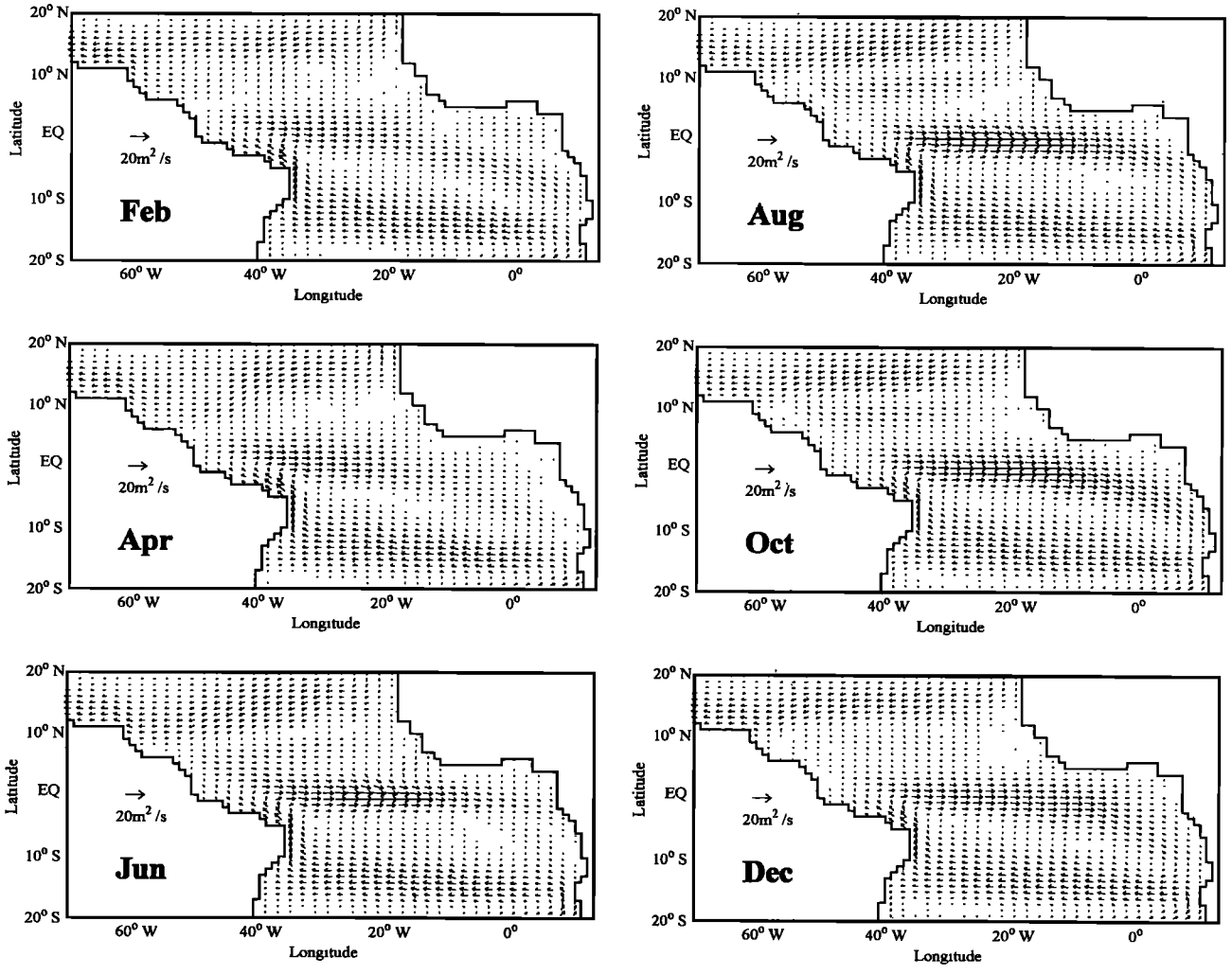

Figure 11. Monthly averaged mass transport (m^2/s) in the thermocline layer from February to December taken from the model result.

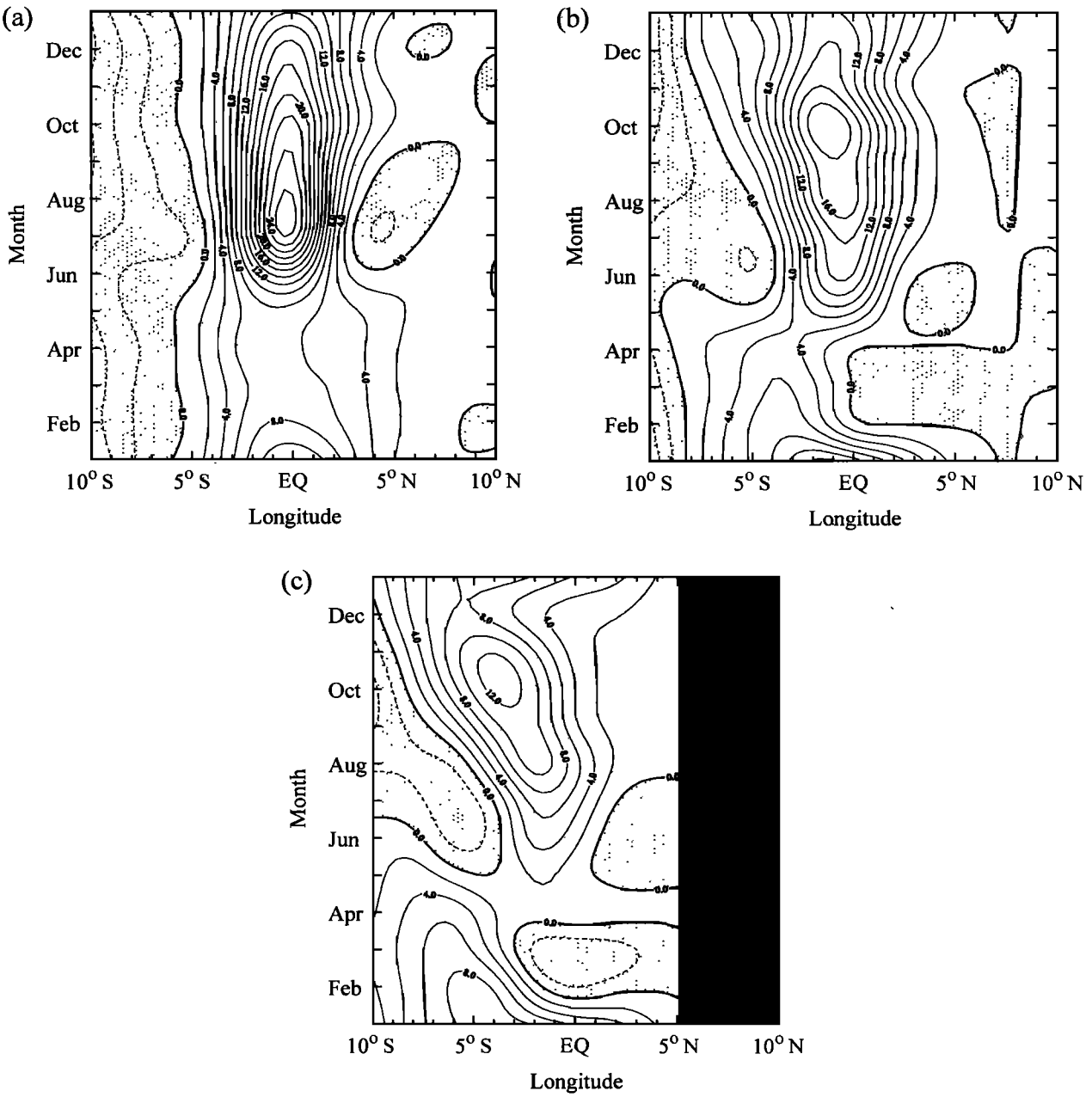

Figure 12. Time-latitude plot of the Equatorial Undercurrent (EUC) across (a) 30°W, (b) 20°W, and (c) 10°W from the model result. The shaded area is negative (westward), and the unit is m^2/s.

3.7. Mixed Layer Diabatic Heat Budget

WWM formation involves actual heating of cold, entrained water. To put this in perspective, we examine the diabatic heat balance in the mixed layer of the model.

The total heat content equation for the mixed layer is

$$\frac{\partial(T_1h_1)}{\partial t}+\frac{\partial}{a\cos\theta\partial\phi}(u_1T_1h_1)+\frac{\partial}{a\partial\theta}(v_1T_1h_1)=\frac{Q}{\rho C_{pw}}+w_eT_2. \quad (22)$$

Multiplying the continuity equation (see (5)) by a constant temperature T_o then subtracting it from (22), we get

$$\frac{\partial[(T_1-T_o)h_1]}{\partial t}+\frac{\partial}{a\cos\theta\partial\phi}[u_1(T_1-T_o)h_1]+\frac{\partial}{\partial\theta}[v_1(T_1-T_o)h_1]=\frac{Q}{\rho C_{pw}}-w_e(T_o-T_2). \quad (23)$$

The heat storage rate of the mixed layer can be divided into two terms:

$$\frac{\partial(T_1h_1)}{\partial t}=\frac{\partial(T_oh_1)}{\partial t}+\frac{\partial[(T_1-T_o)h_1]}{\partial t}. \quad (24)$$

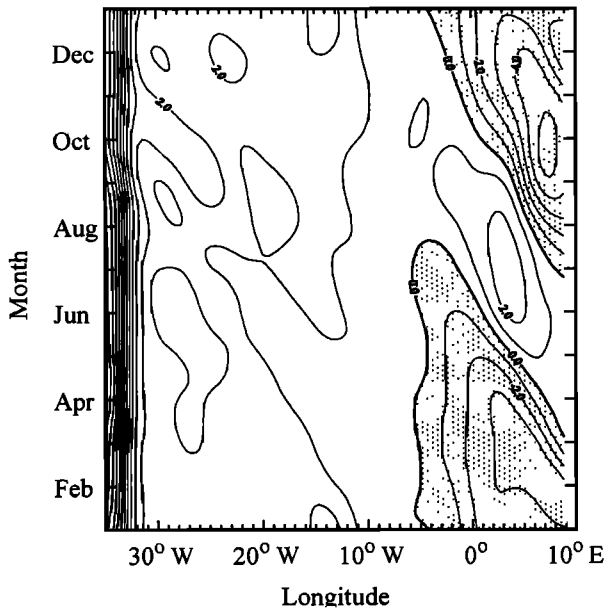

Figure 13. Time-longitude plot of the meridional mass transport in the thermocline layer across 8°S taken from the model result. The shaded area is negative (southward), and the unit is m^2/s.

The first term on the right side describes the change of the heat content not affected by the temperature change in the layer (adiabatic heat change), while the second term represents the change of the heat content with respect to T_o (diabatic heat change). If the T_o indicates the annually and spatially averaged temperature of the mixed layer inside the equatorial cell bounded by the continental lands and the two zonal boundaries (at 8°S and 8°N), (23) becomes the heat content anomaly equation for the mixed layer.

When (23) is integrated over the whole equatorial cell, we get

$$\int_A \frac{\partial[(T_1 - T_o)h_1]}{\partial t} dA - \int_{8°S} \mathbf{v_1} \cdot \mathbf{n} h_1 (T_1 - T_o) dl + \int_{8°N} \mathbf{v_1} \cdot \mathbf{n} h_1 (T_1 - T_o) dl = \int_A \frac{Q}{\rho C_{pw}} dA - \int_A w_e (T_o - T_2) dA, \quad (25)$$

where the unit vector $\mathbf{n}$ represents the vector normal to the southern or northern boundaries. Since these boundaries are both zonal, the normal velocity is meridional. A is the total area of the equatorial cell, and l is the integration path along the zonal boundaries. Figure 15a shows the seasonal variation of the surface heating and the entrainment cooling terms in (25) as given by the model results. The contribution of the diabatic heat anomaly fluxes across the zonal boundaries is negligibly small and is not shown here. Therefore the cycle of the diabatic heat storage rate in the equatorial cell is determined by the local heat balance between the air-sea heat flux and the entrainment cooling. This model result implies that meridional flux of heat into/out of the equatorial cell does not change the mixed layer temperature. However, it must be pointed out that the equatorial ocean still brings much heat northward across 8°N, and this takes place mostly through the transport of mixed layer water of annual mean temperature T_o.

Figure 15a shows that the air-sea heat flux has two maximums in February/March and October and a minimum in April/May. The entrainment cooling prevails only between May and December, with its maximum in June. Accordingly, diabatic heat storage occurs between September and March and escapes during April/August (see Figure 15b). The SST change is roughly out of phase with the diabatic heat storage rate (see Figure 15c); the maximum (minimum) SST occurs when the storage rate changes sign from positive (negative) to negative (positive).

It has been sometimes supposed that the temperature anomaly in the cold water tongue represents the entrainment rate. The heat balance equation (23) shows, instead, that entrainment rate affects the rate of change of surface temperature. A more complete analysis shows a three-way balance among SST change, air-sea heat flux, and entrainment cooling. Therefore the SST change is roughly out of phase with entrainment cooling, except for the influence of air-sea flux. The minimum SST occurs in August/September, and the entrainment rate peaks in June.

The entrainment cooling is responsible for diabatic cooling during May/August, and the air-sea heat flux warms up the mixed layer afterward. As shown in Figure 14a, the WWM escapes mainly after this warm up. Owing to this, the equatorial warm water pool is able to provide more heat toward higher latitudes. Therefore the time lag between the WWM formation and escape increases the efficiency of the equatorial heat engine.

Another interesting point to make is that the diabatic heat accounts for a fairly large portion in the mixed layer heat storage rate and entrainment heat flux. If we multiply $\rho C_{pw} T_o$ ($\sim 1.13 \times 10^8$ J/m^3) with the mixed layer mass storage rate shown in Figure 14c, we get the maximum of about 2.3 PW (if $T_o = 26.4$°C) of adiabatic heat storage rate. The maximum diabatic heat storage rate of -0.8 PW is about 35% of the adiabatic part. Moreover, the annual mean of total heat flux via entrainment is 1.0 PW (see Figure 4b). The diabatic part is about -0.35 PW from Figure 15 (*Niller and Stevenson* [1982] estimated 0.2 PW), which is about 35% of the total. On the other hand, as mentioned, influx/outflux of diabatic heat across the zonal boundaries is negligible. This implies that the surface heat flux is used strictly to warm up the cold entrained water and WWM escape is mainly adiabatic process.

4. Summary and Conclusions

The primary objective of this work was to provide a simple mass and heat balance scenario in the upper tropical Atlantic Ocean, in response to the ITCZ move-

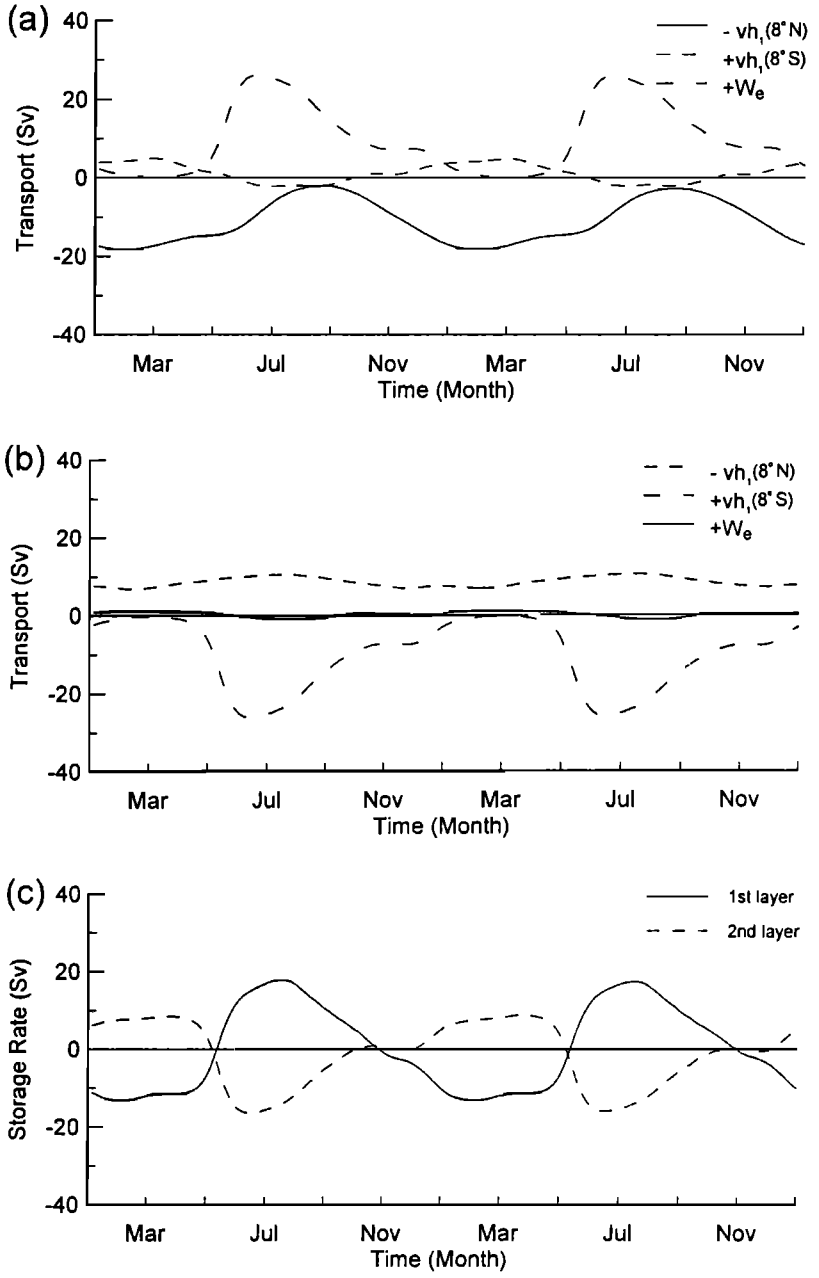

Figure 14. Time changes of the meridional transports of the warm water mass (WWM) integrated along 8°S and 8°N and the entrainment rate integrated between 8°N and 8°S for the (a) mixed layer and (b) thermocline layer. (c) Time change of WWM storage rate integrated between 8°N and 8°S. The unit is in Sv.

ment. A simple 2.5-layer model was forced by seasonally varying climatological wind and heat flux fields. The entrainment from the thermocline to mixed layer was taken to be proportional to the product of the shear stress and interface shear at the bottom of the mixed layer, with the shear stress taken proportional to the wind stress. Important components of heat transport variability were identified and analyzed. Also, physical explanations were attempted. Available observations of the seasonal cycle in the tropical Atlantic were compared with the model results to validate the physical assumptions of the model formulation.

On an annual average, the northward transport of the WWM is about 11 Sv, with roughly 10 Sv associated with entrainment of upper thermocline water, the other 1 Sv coming from the South Atlantic. Out of a total of 10 Sv of the needed upper thermocline water, 9 Sv enters the equatorial cell from the South Atlantic. The principal pathways for the cross-equatorial transport were found to be (1) the Benguela Current, (2) the SEC, (3) the EUC, (4) equatorial entrainment, (5) the NBC, (6) the Guiana Current plus the NECC-NEC, and (7) Caribbean Current, where pathways 1 and 2 take place in the thermocline layer. The modeled transports

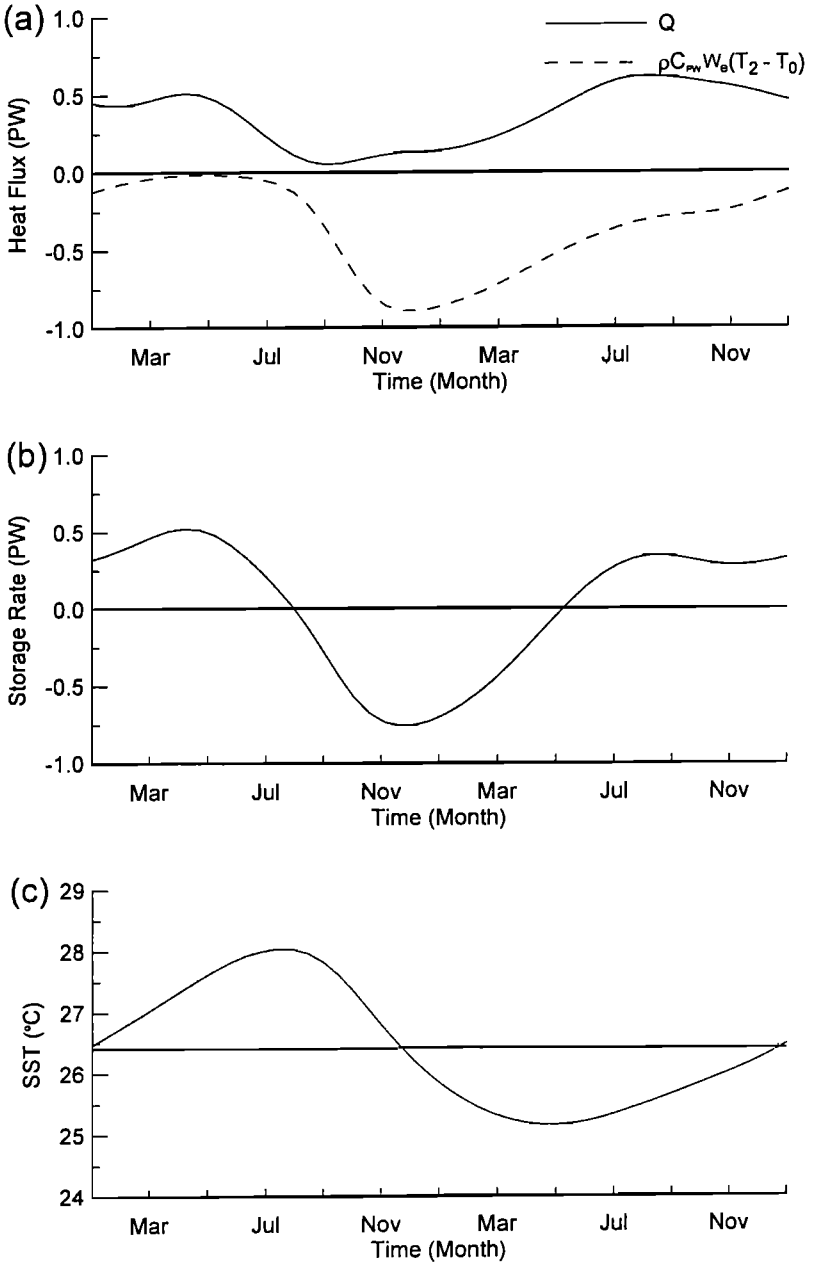

Figure 15. Model-produced (a) net surface heat gain and entrainment cooling and (b) the diabatic heat storage rate, all integrated between 8°S and 8°N and (c) the SST (°C) averaged between 8°S and 8°N.

and their pathways were consistent with observation. It must be reminded that the model is driven mainly by the wind stress, which creates different conditions at the northern and southern boundaries: the thermocline layer depth at the southern boundary becomes shallower than that at the northern boundary. If so, via the mass-restoring device discussed in section 2.5, more water is injected across the southern boundary than across the northern boundary. This is the mechanism how the model achieved 11 Sv of annual mean northward mass transport.

The seasonal response to ITCZ movement was most striking in the entrainment rate and the northward WWM escape rate. The entrainment rate was found to be significant only during May/December and ceased completely between January and March. The locally forced equilibrium response between interface shear and zonal wind stress east of 30°W appears to be responsible for this cycle: during February /April, the ITCZ is located slightly northward of the equator east of 30°W, forming a region of weak zonal wind stress near the equator. Therefore the transports of the SEC and the EUC are also weak, maintaining a low interface shear zone at the equator. In these months, the weak wind stress and shear allow no significant entrainment. As the ITCZ migrates northward after April, the zonal

wind stress near the equator increases, speeding up the westward flowing SEC and pushing more surface water into the western basin, as well as creating a surface layer mass deficit in the east. An additional pressure gradient is then set up below the mixed layer, which in turn increases the speed of the EUC. Consequently, the shear between the mixed layer and the upper thermocline layer increases until the zonal wind stress is relaxed. During May/December, the enhanced wind and shear greatly enhance the entrainment.

The warm water escape rate across 8°N takes place along two pathways, namely, the NBC and the eastern leg of the cyclonic gyre. Further analysis suggests that these two are strongly related to the seasonal intensification of the NECC: during December/April, the NBC flows continuously northwestward as the Guiana Current. The cyclonic gyre, located south of the NEC, transports the warm water mass to the NEC via its eastern leg. During July/September, on the other hand, the strong negative wind stress curl north of 6°N intensifies the NECC and forces the NBC to veer offshore and seal the NBC-Guiana Current connection. At the same time, the increase in the wind stress curl causes a deepening (shallowing) of the mixed layer depth south (north) of the NECC. The northward transport via the eastern leg of the cyclonic gyre is therefore blocked. As a consequence, the tropical warm water pool stores heat during May/October and allows heat to escape in November/April.

Of interest are WWM formation and SST change in response to entrainment and surface heat flux. WWM formation is a two-step process that starts with entrainment of cold, thermocline water followed by heating at the sea surface. On an annual average, heat gain at the sea surface between 8°S and 8°N is about 0.35 PW and is used exclusively to warm up the cold, entrained water, and the heat anomaly fluxes across the zonal boundaries are negligibly small. The seasonal cycle of SST in the equatorial cell consists of a warm season in January/May and a cold season thereafter. Further analysis showed that the cooling of this region from April to August is associated with the low net surface heat gain and intense entrainment cooling. The minimum SST occurs in late August, when entrainment cooling and atmospheric heating cancel each other, allowing zero diabatic heat storage. Entrainment cooling is most intense in early June and decreases thereafter. This reduction of entrainment cooling and increasing atmospheric heating result in net heat gain from September. The WWM escape takes place only after this warm-up.

There is also one very interesting aside on global heat balance: the ITCZ is the thermal equator between hemispheres within which atmospheric heat gain and heat loss balance. In southern winter, the ITCZ is far in the north to allow the atmosphere of the Southern Hemisphere to gain heat from the tropical Atlantic. In northern winter, oceanic heat transport northward supplies enough heat to the atmosphere of the Northern Hemisphere without the ITCZ moving farther south than the equator; but this stoppage of the ITCZ from moving south is what drives the heat storage and northward transport: a positive feedback mechanism.

The 2.5-layer model used in this study may be the simplest possible format for the simulation of the tropical oceans to a reasonable extent. Owing to the straightforward yet simple nature of the model, a few restrictions were imposed. Among those, most significant was the fact that the model covered only the tropical ocean and some part of the subtropical oceans; therefore the remote effects from the higher-latitude oceans were implemented in the model by a simple scheme that adjusted the layer depth at the open boundaries toward their initial values. Accordingly, the influence from the remote part of the oceans played only a passive role, which remains a source of uncertainty in this study. Another point, prompted by a referee, concerns the model grid resolution. The deformation radius of the tropics ranges approximately from 100 to 230 km [*Chelton et al.*, 1998]. The model resolution of 1° therefore marginally resolves the most unstable waves [*Eady*, 1949]. However, small-scale eddies are likely to be distorted by the coarse model resolution, which may be another possible source of error.

Despite these shortcomings, the current 2.5-layer mode study, with the help of the newly suggested entrainment formula, provided the simplest mass balance scenario within the tropical Atlantic Ocean, without any violation of physical principles in this region.

Acknowledgments. The authors would like to thank Paul Schopf, Denny Kirwan, and Chet Grosch for valuable comments on the manuscript. This work was supported by the NOAA, Atlantic Climate Change Program, through a grant entitled "Air-Sea coupling in the North Atlantic," and by the Commonwealth Center for Coastal Physical Oceanography.

References

Cane, M. A., The response of an equatorial ocean to simple wind stress patterns, II, Numerical results, *J. Mar. Res.*, *37*, 253-299, 1979.

Chapman, D. C., Numerical treatment of cross-shelf open boundaries in a barotropic coastal ocean model, *J. Phys. Oceanogr.*, *15*, 1060-1075, 1985.

Chelton, D. B., R. A. deSzoeke, M. G. Schlax, K. El Naggar, and N. Siwertz, Geographical variability of the first-baroclinic Rossby radius of deformation, *J. Phys. Oceanogr.* *28*, 433-460, 1998.

Chen, D., L. M. Rothstein, and A. J. Busalacchi, A hybrid vertical mixing scheme and its application to tropical ocean models, *J. Phys. Oceanogr.*, *24*, 2156-2179, 1994.

Csanady, G. T., Turbulent interface layers, *J. Geophys. Res.*, *83*, 2329-2342, 1978.

Csanady, G. T., What controls the rate of equatorial warm water mass formation?, *J. Mar. Res.*, *45*, 513-532, 1987.

Csanady, G. T., Retroflection and leakage in the North Brazil Current: Critical point analysis, *J. Mar. Res.*, *48*, 701-728, 1990.

Cushman-Roisin, B., *Introduction to Geophysical Fluid Dy-*

namics, 320 pp., Prentice-Hall, Englewood Cliffs, N. J., 1994.

Eady, E. T., Long waves and cyclone waves, *Tellus, 1*, 33-52, 1949.

Esbensen, S. K., and Y. Kushnir, The heat budget of the global ocean: An atlas based on estimate from surface marine observations, *Rep. 29*, 27 pp., Clim. Res. Inst., Oreg. State Univ., Corvallis, 1981.

Ezer, T., and G. L. Meller, Simulation of the Atlantic Ocean with a free surface sigma coordinate ocean model, *J. Geophys. Res., 102*, 15,647-15,657, 1997.

Fleagle, R. G., and A. B. Businger, *An Introduction to Atmospheric Physics*, 432 pp., Academic, San Diego, Calif., 1980.

Gill, A. E., *Atmosphere-Ocean Dynamics*, 662 pp., Academic, San Diego, Calif., 1982.

Gouriou, Y., and G. Reverdin, Isopycnal and diapycnal circulation of the upper equatorial Atlantic Ocean in 1983-1984, *J. Geophys. Res., 97*, 3543-3572, 1992.

Grammeltveldt, A., A survey of finite-difference schemes for the primitive equations for a barotropic fluid, *Mon. Weather Rev., 97*, 384-404, 1969.

Haney, R. L., Surface thermal boundary condition for ocean circulation models, *J. Phys. Oceanogr., 1*, 241-248, 1971.

Hastenrath, S., Heat budget of tropical ocean and atmosphere, *J. Phys. Oceanogr., 10*, 159-170, 1980.

Hastenrath, S., and P. J. Lamb, *Heat Budget Atlas of the Tropical Atlantic and Eastern Pacific Oceans*, 104 pp., Univ. of Wisc., Madison, 1978.

Hellerman, S., and M. Rosenstein, Normal monthly wind stress over the world ocean with error estimates, *J. Phys. Oceanogr., 13*, 1093-1104, 1983.

Hensen, W., Hydrodynamic methods applied to oceanographic problems, paper presented at *Symposium on Mathematical Hydrodynamic Methods for Physical Oceanography*, Inst. Meereskunde, Univ. of Hamburg, Hamburg, Germany, 1962.

Holland, W. R., and L. B. Lin, On the generation of mesoscale eddies and their contribution to the oceanic general circulation, I, A preliminary numerical experiment, *J. Phys. Oceanogr., 5*, 642-657, 1975.

Hsiung, J., Estimates of global oceanic meridional heat transport, *J. Phys. Oceanogr., 15*, 1405-1413, 1985.

Jensen, R. G., A numerical study of the seasonal variability of the Somali current, Ph.D. dissertation, 118 pp., Fla. State Univ., Tallahassee, 1990.

Johns, W. E., T. N. Lee, R. C. Beardsley, J. Candela and R. Limburner, Annual cycle and variability of the North Brazil Current, *J. Phys. Oceanogr., 28*, 103-128, 1998.

Jones, I. S. F., and P. J. Mulhearn, The influence of external turbulence on sheared interface, *Geophys. Astrophys. Fluid Dyn., 24*, 49-62, 1983.

Killworth, P. D., A note on smoothing techniques for leapfrog time-integration schemes, *Ocean Modell., 60*, pp. 5-8, Hooke Inst. Oxford Univ., Oxford, England, 1984.

Kim, J. W., A generalized bulk model of the oceanic mixed layer, *J. Phys. Oceanogr., 6*, 686-695, 1976.

Kraus, E. B., and J. S. Turner, A one-dimensional model of the seasonal thermocline, II, The general theory and its consequences, *Tellus, 19*, 98-105, 1967.

Lee, S.-K., Seasonal variability of heat and mass transport processes in the upper tropical Atlantic Ocean: A numerical model study, Ph.D. dissertation, 112 pp., Old Dominion Univ., Norfolk, Va., 1995.

Lee, S.-K., and G. T. Csanady, Warm water formation and escape in the upper tropical Atlantic Ocean, 1, A literature review, *J. Geophys. Res.*, this issue.

Levitus, S., Climatological atlas of the world ocean, *NOAA Prof. Pap. 13*, 173 pp., U.S. Gov. Print. Off., Washington, D.C., 1982.

Lilly, D. K., On the computational stability of numerical solutions of time-dependent non-linear geophysical fluid dynamic problems, *Mon. Weather Rev., 93*, 76-84, 1965.

Lofquist, K., Flow and stress near an interface between stratified liquids, *Phys. Fluids, 3*, 158-175, 1960.

McCreary, J. P., and Z. Yu, Equatorial dynamics in a 2.5 layer model, *Prog. Oceanogr., 29*, 61-132, 1992.

Niiler, P., and J. Stevenson, The heat budget of tropical ocean warm-water pools, *J. Mar. Res., 40*, suppl., 465-480, 1982.

Orlanski, I., A simple boundary condition for unbounded hyperbolic flow, *J. Comput. Phys., 21*, 251-269, 1976.

Philander, S. G. H., and R. C. Pacanowski, A model of the seasonal cycle in the tropical Atlantic ocean, *J. Geophys. Res., 91*, 14,192-14,206, 1986.

Roemmich, D., The balance of geostrophic and Ekman transports in tropical Atlantic ocean, *J. Phys. Oceanogr., 13*, 1534-1539, 1983.

Sarmiento, J. L., On the north, and tropical Atlantic heat balance, *J. Geophys. Res., 91*, 11,677-11,689, 1986.

Schopf, P. S., and M. A. Cane, On equatorial dynamics, mixed layer physics and sea surface temperature, *J. Phys. Oceanogr., 13*, 917-935, 1983.

Servain, J., and D. M. Legler, Empirical orthogonal function analysis of tropical Atlantic sea surface temperature and wind stress: 1964-1979, *J. Geophys. Res., 91*, 14,181-14,191, 1986.

Shuman, F. G., Numerical methods in weather prediction, II, Smoothing and filtering, *Mon. Weather Rev., 85*, 357-361, 1957.

Voituriez, B., and A. Herbland, The use of the salinity maximum of the equatorial undercurrent for estimating nutrient enrichment and primary production in the Gulf of Guinea, *Deep Sea Res., Part A, 26*, 77-83, 1979.

G. T. Csanady,4771 S. Prairie Hills Drive, Green Valley, AZ 85614.

S.-K. Lee, Maritime Research Institute, Samsung Heavy Industries, 530, Jangpyung-Ri, Shinhyun-Up, Koje-City, Kyungnam, 656-800, Korea. (sklee621@hanmail.net)

(Received November 25, 1997; revised March 1, 1999; accepted March 9, 1999.)